Synthesis and structural analysis of *push-pull* imidazole-triazole based fluorescent bifunctional chemosensor for Cu^{2+} and Fe^{2+} detection

Ana Da Lama [a], José Pérez Sestelo [a], Laura Valencia [b], David Esteban-Gómez [a,**], Luis A. Sarandeses [a,***], M. Montserrat Martínez [a,*]

[a] Centro de Investigacións Científicas Avanzadas (CICA) and Departamento de Química, Universidade da Coruña, E-15071, A Coruña, Spain
[b] Departamento de Química Inorgánica, Facultad de Ciencias, Universidade de Vigo, E-36310, Vigo, Spain

A B S T R A C T

Fluorescent imidazole-triazole based ligands **L1** and **L2** have been designed as chemical *push-pull* chemosensors for divalent metal ions and synthesized through palladium-catalyzed cross-coupling reactions using indium organometallics and click chemistry. The novel ligands exhibit intense absorption in the ultraviolet region with high molar extinction coefficients, and strong fluorescence emission with large Stokes displacements. On the basis of UV–Vis absorption spectroscopy and fluorescence emission data in acetonitrile, **L1** is shown as a bifuncional chemosensor with differential response for Fe^{2+} and Cu^{2+} over a range of selected 3*d* divalent and other metal ions. The binding site of the ligand was established by single-crystal X-ray diffraction and ^{1}H NMR spectroscopy studies. The association constants, determined by spectrofluorimetric titrations, show a steady binding affinity of **L1** for Cu^{2+} and Fe^{2+} in comparison with other previously reported fluorescent bidentate chemosensors, offering the lowest limit of detection (LOD) with Cu^{2+}. DFT calculations provide a rationale properly understanding and interpreting the experimentally observed results. Indeed, a mechanism of the different optical responses of **L1** towards 3*d* divalent metal ions is proposed.

1. Introduction

Iron and copper are among the most important metals involved in living systems, [1] playing important roles as cofactors in metalloproteins and in different neurological processes. [2] Imbalance of copper and iron in an organism can induce toxicity in cells causing undesirable diseases. For example, disruption of iron regulation has been linked to disorders such as anemia, hemochromatosis and Alzheimer's disease. [3] On the other hand, dysregulation of copper homeostasis is associated with neurodegenerative disorders like amyotropic lateral sclerosis, Menkes's, Parkinson's and Wilson's diseases. [4] As a result, the development of organic small-molecules as sensitive and selective sensors in detection of Cu^{2+} and Fe^{2+} metal ions has raised remarkable interest, and in particular, fluorescent chemosensors due to their multiple advantages including high selectivity, high sensitivity, low detection limit and easy operation. [5,6]

The interaction of fluorescent chemosensors with ions led to the perturbation of the electronic cloud density and distribution or molecular rotation in the fluorophores, which may initiate photophysical processes such as intramolecular charge transfer (ICT), photoinduced electron transfer (PET), fluorescence resonance energy transfer (FRET), metal-ligand charge transfer (MLCT), and aggregation-induced emission (AIE). [7] So far, most of the chemosensors that have been developed for the Cu^{2+} and Fe^{2+} recognition exhibited "turn-off" fluorescence response, [8] and in general, this quenching event is attributed to the PET mechanism. [9] In addition, most of these organic sensors usually selectively respond to Cu^{2+} or Fe^{2+} ions by a single mode. Bi- and multifluorescent ion chemosensors [10] based on different fluorescence mechanism which can simultaneously respond to divalent Cu^{2+} and Fe^{2+} metal cations are seldom reported (Fig. 1a). [11]

Imidazole derivatives have attracted a great deal of interest as fluorescent chemosensors owing to the presence of a coordinating pyridine-like nitrogen atom in its structure [12]. In addition, its backbone facilitates the internal electron transfer in donor-acceptor-type ICT
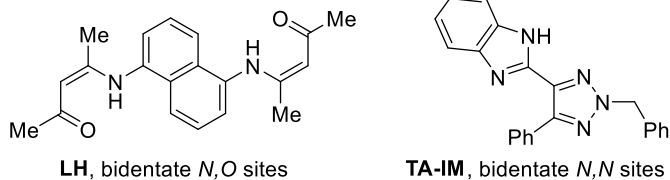
---

a) Previous work

On/Off fluorescent chemosensor for Fe^{2+} and Cu^{2+} (**LH**) and **TA-IM** derivative fluorescent probe for Ag$^+$ detection

LH, bidentate *N,O* sites   **TA-IM**, bidentate *N,N* sites

b) This work

Bifunctional chemosensor for Fe^{2+} and Cu^{2+} (**L1**)

L1, **L2** bidentate *N,N* sites

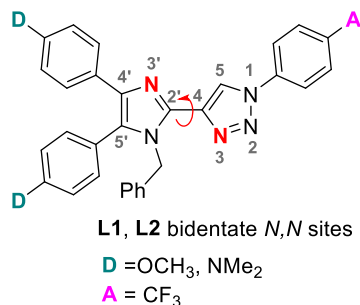**D** =OCH$_3$, NMe$_2$
A = CF$_3$

Fig. 1. (a) Reported chemosensor **LH** and fluorescent probe **TA-IM**. (b) Structure of fluorophores investigated in this article.

sensors, whose optical response can be modulated by changing the nature of the electron-withdrawing or electron donating groups attached to the C(2) or C(4)/C(5) positions of the imidazole fragment. Taking this into account, the imidazole ring could be connected to different heterocycles, giving rise to π-conjugated systems that offer binding sites for the detection of transition metal ions. [13] In this context, the 1,2,3-triazole ring is an aza-heterocycle easily accessible via Cu(I)-catalyzed azide-alkyne cycloaddition. [14] The resulting 1,2,3-triazoles could perform different roles in a sensor, either in the recognition of metal ions through one of their nitrogen donor atoms or, less frequently, as a linker in the conjugate backbone of *push-pull* fluorophore. [15] In some cases, *push-pull* chromophores incorporating triazole rings as linkers have been reported to show low to moderate fluorescent properties. However, some of them show a switchable fluorescence, being activated by the addition metal cations. [16]

Although a number of chemosensors either based on imidazole or 1,2,3-triazole moiety have been developed for detection of divalent transition metal cations, bidentate imidazole-triazole ligand is still rather rare. Hitherto, only a 1,2,3-triazole-benzo[*b*]imidazole derivative (TA-IM, Fig. 1a) was reported as a fluorescent active compound with selectivity toward Ag$^+$ ions. [17] In this system, the incorporation of an intramolecular H-bond between the imidazole and triazole moiety is necessary to enhance the formation of a co-planar conformation to achieve fluorescence emission. Therefore, the development of chemosensors based on bidentate nitrogen binding mode capable of recognizing transition metal ions with differential fluorescence response remains a challenge. Herein, we report the synthesis of new chemosensors for divalent metal ions of biological interest based on *push-pull* imidazole-triazole core and their photophysical properties and chemosensory ability (Fig. 1b).

2. Results and discussion

2.1. Synthesis

Ligands **L1** and **L2** were designed based on the fluorogenic properties

of the (4-trifluoromethyl)phenyl-1,2,3-triazole as an electron-withdrawing subunit and the chelating binding mode resulting from its combination with an imidazole core linked at the C(2′) position. During the design of the ligands, electron-donating groups such as 4-methoxy- or 4-(*N,N*-dimethylamino)phenyl, were envisioned at the imidazole ring at C(4′) and C(5′) positions, to obtain a larger electron delocalization that should enhance the ICT along the π-system (Fig. 1b). These electronic features and the structural placement of the donor atoms, should allow the study of the interaction of **L1** and **L2** with different metal ions by following the changes in their photophysical properties.

Usually, the synthesis of imidazole derivatives is performed by the construction of the imidazole scaffold through condensation reactions. [18] One alternative pathway are cross-coupling reactions involving halogenated imidazoles, although examples are rare due to the electronic character of the imidazole ring. [19] With this regard, in recent years we have demonstrated that triorganoindium reagents (R$_3$In) are effective in palladium-catalyzed cross-coupling reactions with 2,4,5-triodoimidazole for the synthesis of bioactive neurodazine and analogues. [20] Our experience using R$_3$In in the synthesis of bioactive heterocyclic compounds and organic materials [21], led us to explore the ability of R$_3$In reagents in the synthesis of *push-pull* imidazole-triazole ligands. The synthesis of **L1** and **L2** was planned by selective and sequential Pd-catalyzed cross-coupling reactions of triorganoindium reagents with 1-benzyl-2,4,5-triodoimidazole (**1**), followed by Cu(I)-catalyzed azide-alkyne cycloaddition as key steps (Scheme 1).

Based in our experience in cross-coupling reactions, we tried the reaction of **1** with tris(trimethylsilylethynyl)indium in the presence of Pd(PPh$_3$)$_4$ (5 mol%) obtaining the monocoupling product selectively at C(2') position in 57% yield (**2**, Scheme 1). Next, a two-fold palladium-catalyzed cross-coupling reaction of **2** with tri(4-methoxyphenyl)indium (100 mol%) using the same catalytic system provided the double coupling product **3a** in 63% yield. Using this approach, compound **3b** was obtained from **2** and tris[(4-(*N,N*-dimethylamino)phenyl)]indium in 60% yield. The utility and effectiveness of R$_3$In (transfer more than one group attached to the metal) in the reaction with **1** was also demonstrated in the sequential Pd-catalyzed cross-coupling reaction in one vessel by successive addition of the two organoindium reagents, without the need to add an additional amount of catalyst, affording **3a** in 31% overall yield. The last steps of the synthesis require the removal of the silyl group and formation of the triazole ring by click reaction. Thus, the basic treatment of trisubstituted imidazoles **3a** and **3b** gave the corresponding terminal alkynes **4a** and **4b** in good yields (89% and 88%, respectively). Finally, Cu(I)-catalyzed azide-alkyne cycloaddition (CuAAC) reaction of **4a** and **4b** with 1-azido-4-(trifluoromethyl)benzene in presence of sodium ascorbate and copper sulfate afforded **L1** and **L2** in 70% and 76% yield respectively (Scheme 1).

2.2. Single crystal X-ray structures of [(H**L2**)·ClO$_4$] and [Zn(**L2**)Cl$_2$]

To gain insight into the ligands behaviour towards the selected metal ions, we have performed crystallization attempts of **L1** and **L2** with different metal salts in various metal:ligand ratio at room temperature. Crystals of the [(H**L2**)·ClO$_4$] hydrogen-bond adduct (Fig. 2a) show an almost planar conformation in the ligand backbone that favors the ICT responsible of its photophysical properties. One of the dimethyl aminophenyl substituents, the imidazole ring and the trifluoromethylphenyl unit are coplanar, while the 1,2,3-triazole ring is slightly folded with respect to them with a dihedral angle of 18.56°. On the other hand, the solid state structure of the [Zn(**L2**)Cl$_2$] complex (Fig. 2b) shows a 1:1 stoichiometry (M:L) for the resulting complex.

It is remarkable the fact that in the[Zn(**L2**)Cl$_2$] complex, the imidazole and 1,2,3-triazole rings are rotated with respect to the previous conformation observed in the [(H**L2**)·ClO$_4$] hydrogen-bond adduct. This reorganization allows the ligand to act in a bidentate chelating mode, where the Zn(1)-N(3-') distance (2.043(3) Å) is slightly shorter than the
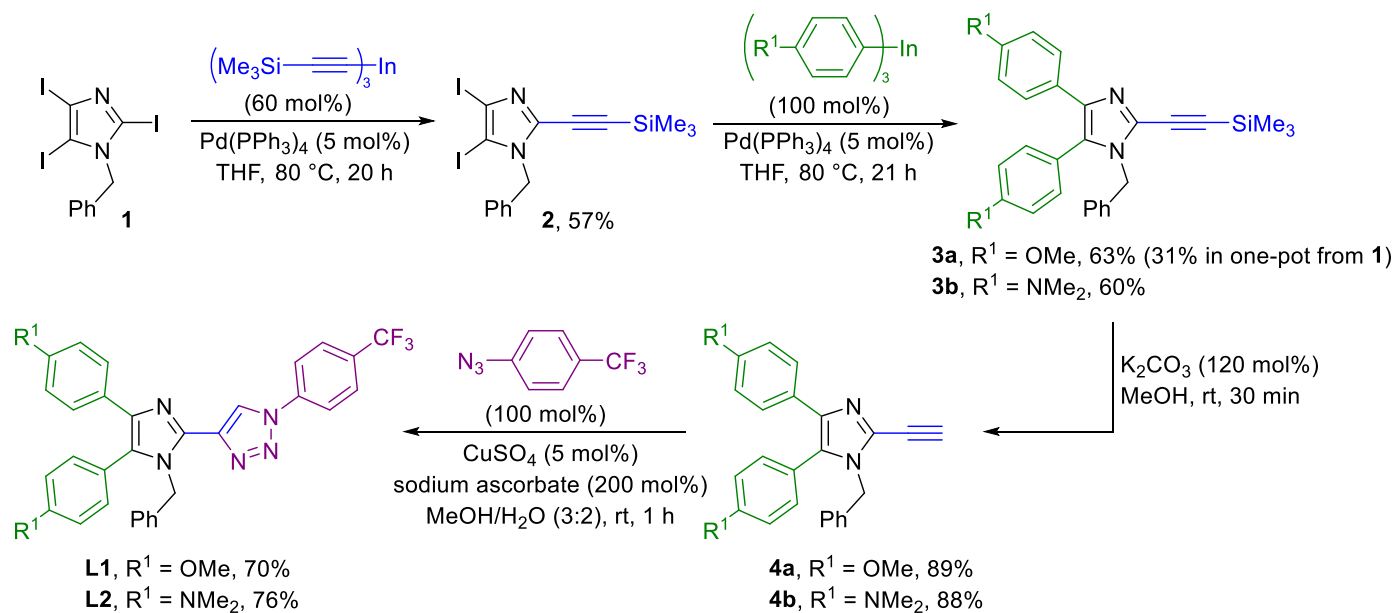
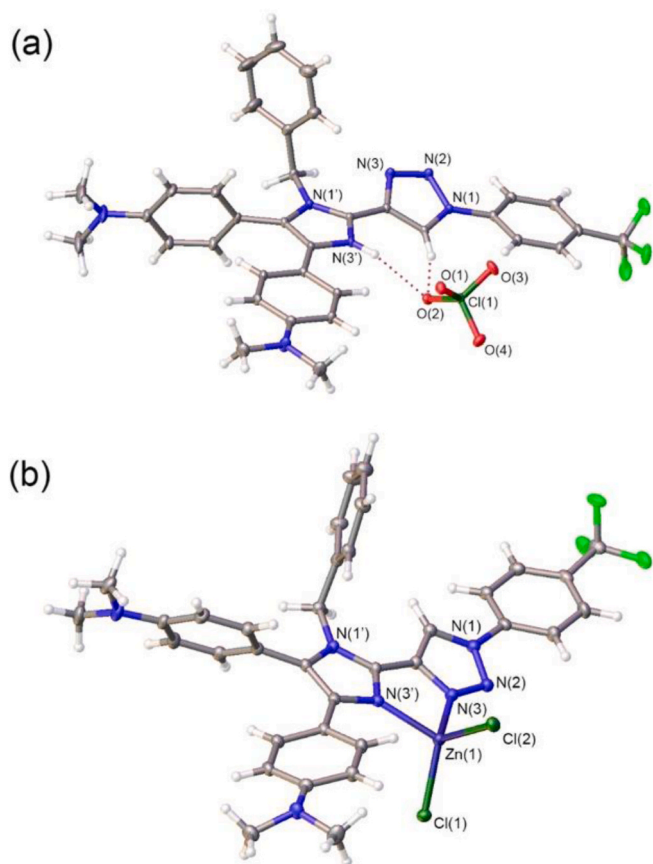**Scheme 1.** Synthetic route to ligands **L1** and **L2**.

Fig. 2. (a) X-ray molecular structure of the [(H**L2**)·ClO₄] hydrogen-bond adduct (*anti* conformation). The ORTEP plot is at the 30% probability level. (b) X-ray molecular structure of the [Zn(**L2**)Cl₂] complex (*syn* conformation). The ORTEP plot is at the 30% probability level.

Zn(1)–N(3) (2.144(3) Å). Unlike the [(H**L2**)·ClO₄] hydrogen-bond adduct, the organic backbone in [Zn(**L2**)Cl₂] exhibits a loss of planarity, in which the rest of the aromatic rings are folded in a different manner with the imidazole-Zn-triazole plane. Full details of the C–C and

C–N bond lengths and angles as well as the hydrogen bond interactions and the crystal packing data are given in the Supplementary Data (Fig. S1 and Tables S1 and S2).

2.3. Conformational study by ¹H NMR

According to the X-ray crystal structures described above, two different planar conformations, named *syn* or *anti* depending on the relative orientation between N(3')$_{imid}$ and N(3)$_{triaz}$ in the ligand backbone, may be observed due to the internal rotation along the imidazole-triazole axis. In the *syn* conformation, lone pairs of these nitrogen atoms should be facing each other, whereas in the *anti* conformation they are located on opposite sides of the imidazole-triazole core. In fact, the *anti* conformation avoids the electron lone pairs repulsion, giving rise to a more favoured conformation that could also be stabilized by an intra-molecular hydrogen bond between the imidazole N(3') and the H(5) of the triazole unit (on top of Fig. 3). To gain further insight into the conformational behaviour of **L1** and **L2** the ¹H NMR spectra of both ligands were recorded in different polarity solvents. The ¹H NMR spectrum of **L2** in CDCl₃ showed the presence of a single species in solution, suggesting that the higher π delocalization over the aromatic backbone from one 4-(*N,N*-dimethylamino)phenyl group to the imidazole-triazole moiety could also help to stabilize the *anti* conformation (Fig. S3d). The ¹H NMR of **L1** in CDCl₃ reveals a broadening of the hydrogen-signals along with the presence of a new set of signals. This may be attributable to the presence of a minor species in solution, indicative of a dynamic interconversion process likely involving *anti* and *syn* conformations (Fig. S2b). This result can be explained on the basis to the presence of a less electron donating group (methoxy) in **L1** which may reduce the π delocalization favoring a less rigid structure.

When the ¹H NMR spectra of **L1** and **L2** were recorded in a more polar solvent such CD₃CN, H(5) shows a significant low field shift from 8.71 to 8.96 ppm in **L1** and from 8.78 to 9.15 ppm in **L2** (Figs. S2a and S3c respectively). It seems that the interaction with a more polar solvent may decrease the rotational barrier around the imidazole-triazole axis and thus reducing the intramolecular hydrogen bond with N(3')$_{imid}$ in a *syn* conformation. Although it cannot be ruled out that the polarization of the C(5)–H(5) bond in the triazole ring, and the consequent downfield shift, could also be induced by a through space effect due to a strong interaction of H(5) with the solvent.

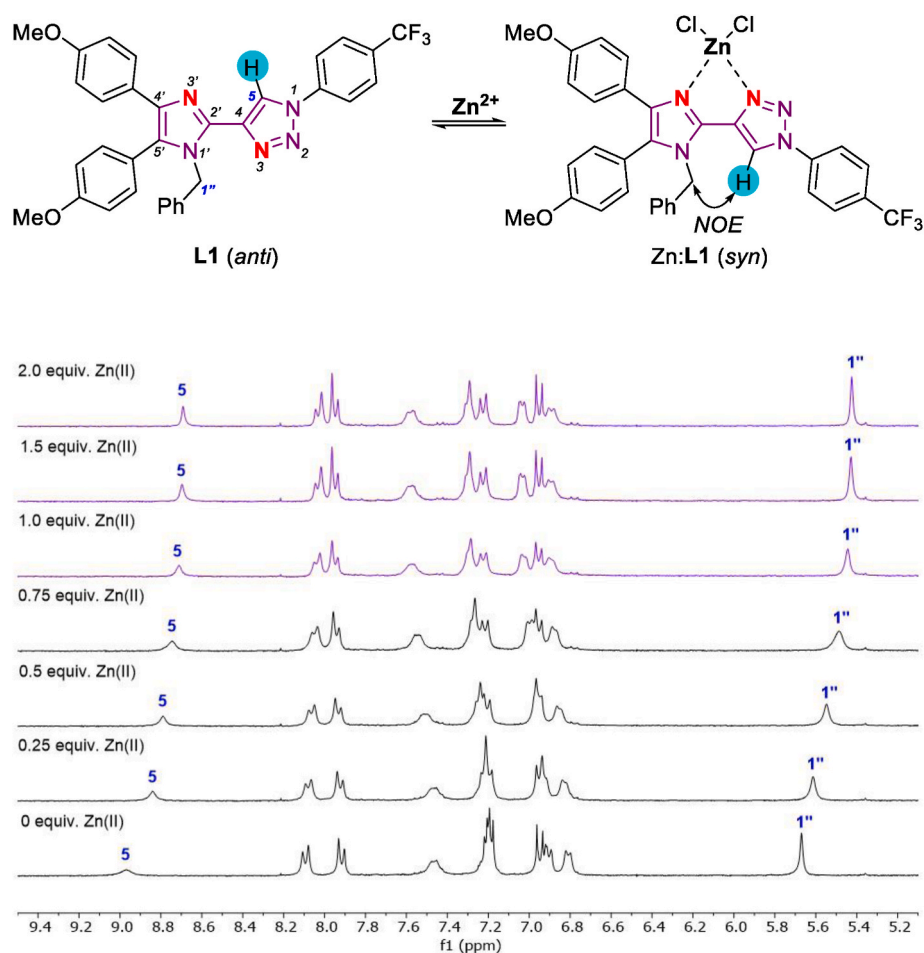To elucidate the binding mode of the ligands, a ¹H NMR spectroscopy

Fig. 3. ^{1}H NMR titration of **L1** ($8.6 \cdot 10^{-3}$ M, CD$_3$CN) upon addition of ZnCl$_2$ (up to 2 equiv.).

titration experiment of **L1** with incremental addition of Zn^{2+} from 0.25 to 1 equivalent in CD$_3$CN was carried out (Fig. 3). The signal of H(5) of the triazole ring at 9.0 ppm shifted upfield to 8.75 ppm, and the H(1") of the benzyl group show an upfield shift from 5.7 to 5.5 ppm, which is indicative of the coordination of the Zn^{2+} to the triazole and imidazole moieties (Fig. S4). Upon increasing the concentration of Zn^{2+} ion above 1 equivalent, the signals remain practically unchanged, indicating the formation of a stable complex between **L1** and Zn^{2+} and confirming in 1:1 (M:L) stoichiometry.

In addition, NOESY experiments were performed in CD$_3$CN with **L1** and the Zn:**L1** complex. The lack of NOE effect between H(5) of the triazole unit and the bencylic hydrogens H(1") in **L1** and the NOE correlation between H(5) and H(1") in the Zn:**L1** complex, confirm the *anti* conformation in the ligand at the beginning of the titration (Figs. S5 and S6 respectively). Overall, both ^{1}H NMR titration of **L1** and NOESY experiments of **L1** and Zn:**L1** complex are consistent with the solid state structures, where an internal reorganization from the *anti* to *syn* conformation is required to allow a bidentate chelate coordination mode.

2.4. Optical properties

The optical properties of **L1** and **L2** were measured in various solvents (Fig. 4). The UV–Vis absorption spectra are dominated by two intense π→π* electronic transitions, ligand centered (LC) or ICT, in all solvents (Table S3). These bands may present a slight red or blue-shift depending on the polarity of the solvent. In CHCl$_3$, the spectra show broad and low intensity absorptions due to n→π* transitions at 410 and 425 nm for **L1** and **L2**, respectively. These weak bands are

hypsochromatically shifted and almost hidden under the intense π→π*transitions for both systems in the more polar solvents (Fig. 4a and b and Table S3).

The fluorescence spectra of both ligands were also registered in the same solvents. In the case of **L1**, the emission band showed a positive solvatochromic effect, with a gradual bathochromic shift from 424 to 497 nm as the solvent polarity increased (Fig. 4a). This behavior is typical of compounds where the emission process is associated with an ICT transition, and indicates that the emissive excited state has a larger dipole moment than the ground state. [22] Interestingly, the emission band in MeOH is blue-shifted with respect to its position in CH$_3$CN and quenching of the fluorescence emission also occurs. This fact is related with the protic nature of this solvent, that allows it to establish inter-molecular hydrogen bonding interactions with lone-pair-electrons of the methoxy group in the ground state, as well as with nitrogen atoms of the imidazole-triazole core in the excited state, quenching the emission via non-radiative pathways. An enhanced solvatochromic effect is observed in the case of **L2** (Fig. 4b). The presence of a more electron-donating group such as 4-(*N,N*-dimethylamino)phenyl substituent, favors a more extended π-conjugated network in the ligand backbone and facilitates charge transfer upon excitation. This results in a larger bathochromic shift of the emission maxima in CHCl$_3$ with respect to that observed for **L1**, indicating that **L2** exhibits a strongly dipolar excited state in comparison with **L1**. Consequently, the solvent polarity effect is higher in the latter and the fluorescence emission is quenched not only in MeOH, but also in non-protic polar solvents such as CH$_3$CN or even in a less polar one such as EtOAc. Thus, the introduction of electron-donating groups (4-*N,N*-dimethylaminophenyl) in **L2** favors a more extended π-conjugated system, which significantly lowers the
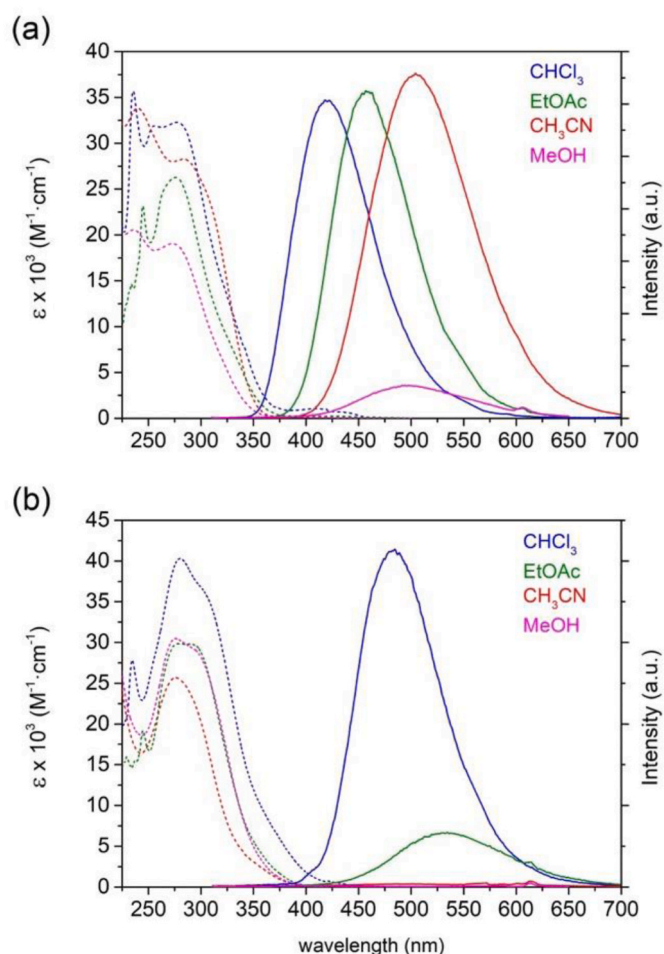
Fig. 4. (a) Absorption (dot line) and emission spectra (continuous line) of **L1** in different organic solvents. (b) Absorption (dot line) and emission spectra (continuous line) of **L2** in different organic solvents.

HOMO-LUMO energy gap in CH_3CN, promoting non-radiative deactivation pathways from the ICT excited state.

In view of these results, a more detailed study of the optical properties of both ligands was carried out in $CHCl_3$. As mentioned above, the presence of a stronger electron-donor group in **L2** leads to a more efficient electron delocalization, resulting in a longer λ_{max} absorption value of 305 nm (278 nm for **L1**) and a larger molar absorption coefficient of 36144 M^{-1} cm^{-1} (27163 M^{-1} cm^{-1} for **L1**), which is indicative of its higher absorption capacity with respect to **L1** (Table 1). A similar trend of the emission wavelength maxima is also observed, where photoexcitation of the ligands leads to the appearance of the ICT emission bands centered at 424 and 484 nm for **L1** and **L2**, respectively. The large Stokes shift values observed for both ligands, 146 and 179 nm for **L1** and **L2** respectively, are indicative of significant differences (vibrational, electronic, geometric) between the ground state and the excited state, which

Table 1

UV–Vis and PL data of **L1** and **L2** in $CHCl_3$.

Comp.[a]	λ_{max}^{Abs} (nm) ($\varepsilon(M^{-1}\ cm^{-1})$)	λ_{max}PL (nm)	Stokes shift (nm)	Φ_F[b]
L1	255 (26651), 278 (27163)	424	146	0.15
L2	280 (39271), 305 (36144)	484	179	0.14

[a] All spectra were recorded in $CHCl_3$ solutions at room temperature at $2.0 \cdot 10^{-6}$ M for UV–Vis and PL spectra.

[b] Fluorescence quantum yield determined relative to quinine sulfate in H_2SO_4 (0.1 M) as standard ($\Phi_F = 0.55$); excitation at $\lambda = 278$ and 280 nm.

implies substantial excited state relaxation in the molecules due to weak structural rigidity. [23] These values should contribute to minimize possible self-quenching improving the optical response of the probes, but the relatively low quantum yields obtained for **L1** and **L2** (0.15 and 0.14, respectively), suggest a high energy loss through non-radiative deactivation pathways from the excited state in both cases (Fig. S14). [24]

Finally, the CIE chromaticity coordinates of the ligands were calculated to be (0.1996, 0.2123) for **L1** and (0.2129, 0.3417) for **L2**, (Fig. S18), in accordance with the color displayed by these two chromophores upon excitation.

2.5. Metal ion sensing properties

The binding ability of **L1** towards different divalent first row transition metal ions (Mn^{2+}, Fe^{2+}, Co^{2+}, Ni^{2+}, Cu^{2+} and Zn^{2+}) and other representative metal ions such Na^+, Mg^{2+}, Hg^{2+} and Ag^+ in solution was investigated using UV–Vis absorption and/or fluorescence emission spectroscopies. CH_3CN was selected as the solvent due to the lack of solubility of the metal salts object of our study in other less polar solvents. As previously mentioned, CH_3CN quenches the emission fluorescence of **L2**, so we decided to exclude this ligand from the recognition study.

2.5.1. UV–vis spectroscopic studies and binding stoichiometry

Our sensing study of **L1** started with the spectrophotometric titrations with Mn^{2+}, Ni^{2+} and Zn^{2+} in CH_3CN (Fig. 5). Under the experimental conditions, the symmetric *d*-shell electronic configurations of these metal ions in an octahedral environment (d^5, d^8 or d^{10}, respectively) allowed the performance of all the spectrophotometric titrations without any interference associated to the presence of very weak forbidden *d-d* transitions in a large excess of metal ion. No metal-to-ligand or ligand-to-metal charge transfer (MLCT or LMCT) were observed during the titrations, indicating that upon photoexcitation, the electronic charge does not shift between the ligand and the coordinated metal ions. In the case of Zn^{2+} and Mn^{2+} a similar behaviour of the ligand absorption band centered at 284 nm is observed, which progressively decreases while a new band forms and develops at longer wavelengths (Fig. 5a and b respectively). The presence of sharp and simultaneous isosbestic points at 295 and 330 nm for Mn^{2+} or a single one at 295 nm for Zn^{2+} indicates that only two species coexist at the equilibrium in both cases. The best fits of the titration data were obtained by assuming the existence of one equilibrium, according to the formation of a 1:1 [M:**L1**] species in solution. The smooth titration profiles and the large excess required of Mn^{2+} or Zn^{2+} to provoke a significant formation of the complexes reflect a weak interaction between **L1** and the cations.

In the case of Ni^{2+}, the family of spectra recorded during the titration with different isosbestic points and distinct evolution patterns of the absorption bands, indicates a more intricate behaviour with a higher number of species coexisting at the equilibrium (Fig. 5c). The high resolution mass spectra recorded by electrospray ionization (ESI-MS) for solutions of **L1** in the presence of 0.5 and 1 equivalents of $Ni(ClO_4)_2$ (Fig. S30) show peaks due to the 1:1, 1:2 and 1:3 [Ni:**L1**] entities. Thus, the titration profile was fitted assuming the existence of three stepwise equilibria.

2.5.2. Fluorescence emission studies and binding stoichiometry

Later spectrofluorimetric titrations of **L1** upon addition of Zn^{2+}, Mn^{2+} and Ni^{2+} were performed. We found that the fluorescence emission band of the ligand centered at 500 nm is quenched upon addition of Zn^{2+} or Ni^{2+}, whereas a blue-shift of this band (57 nm) is observed during the titration with Mn^{2+}, with a defined isosbestic point at 480 nm (Figs. S19–S21).

To our surprise, these different two responses were also observed during the spectrofluorometric titration of **L1** with other metal ions such
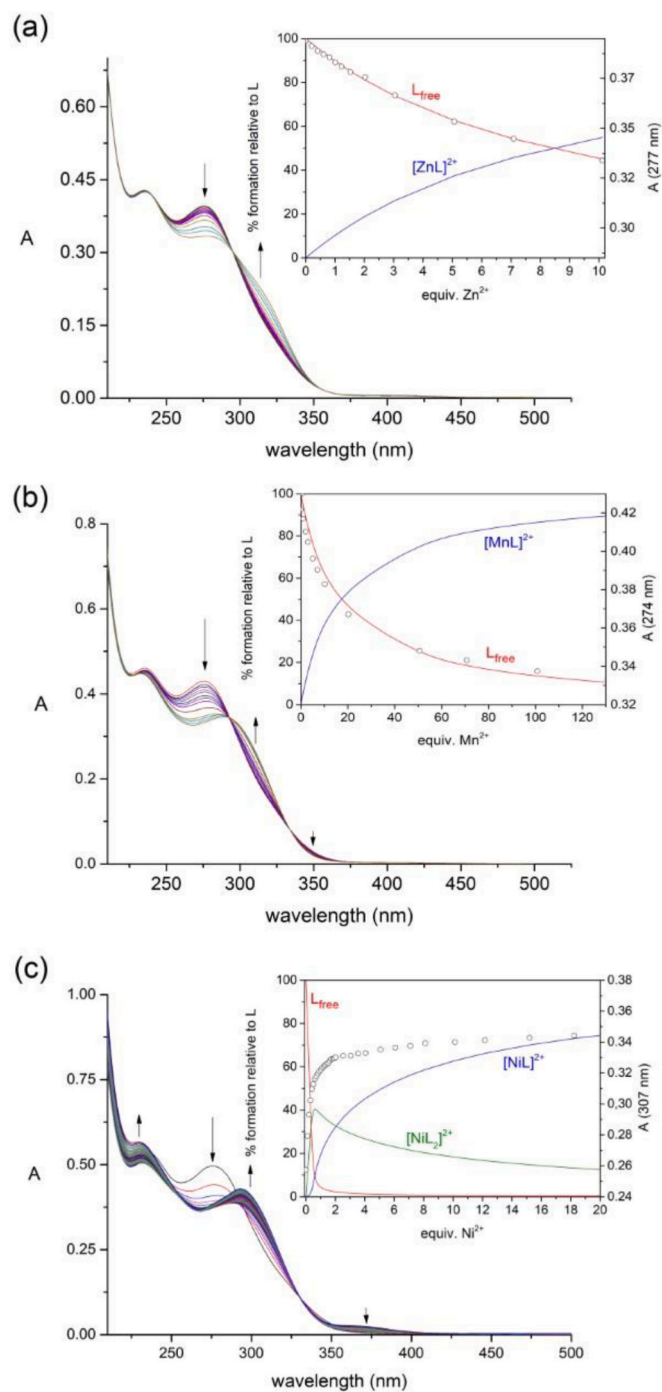
Fig. 5. (a) UV–Vis titration of L1 ($1.52 \cdot 10^{-5}$ M in CH$_3$CN) with ZnCl$_2$ (1–50 equiv.). (b) UV–Vis titration of ligand L1 ($1.63 \cdot 10^{-5}$ M in CH$_3$CN) with Mn(ClO$_4$)$_2$ (0–130 equiv.). (c) UV–Vis titration of ligand L1 ($1.88 \cdot 10^{-5}$ M in CH$_3$CN) with Ni(ClO$_4$)$_2$ (1–130 equiv.). The insets show the titration profile and the corresponding species distribution diagram obtained for each experiment.

Fig. 6. (a) Emission spectra registered in the course of the titration of ligand L1 ($2.49 \cdot 10^{-6}$ M in CH$_3$CN) with CoCl$_2$ (0–210 equiv.). (b) Emission spectra registered in the course of the titration of ligand L1 ($2.41 \cdot 10^{-6}$ M in CH$_3$CN) with Fe(ClO$_4$)$_2$·6H$_2$O (0–150 equiv.). (c) Emission spectra registered in the course of the titration of ligand L1 ($2.48 \cdot 10^{-6}$ M in CH$_3$CN) with Cu(ClO$_4$)$_2$ (0–220 equiv.). The inset shows the titration profile and the corresponding species distribution diagram.

as Co^{2+}, Fe^{2+} and Cu^{2+}, which could not be studied following the changes of the UV–Vis absorption spectra due to the interference of the more intense *d-d* transitions of these metal ions. The addition of Co^{2+} promotes the quenching of the emission, while an unusual blue-shift of 61 nm for Fe^{2+} occurs (Fig. 6a and b respectively). It should be noted that **L1** showed an unusual (turn-on-blue-shift) optical response towards Fe^{2+} in comparison to other reported chemosensors based on imidazole moiety [10b-c,-25].

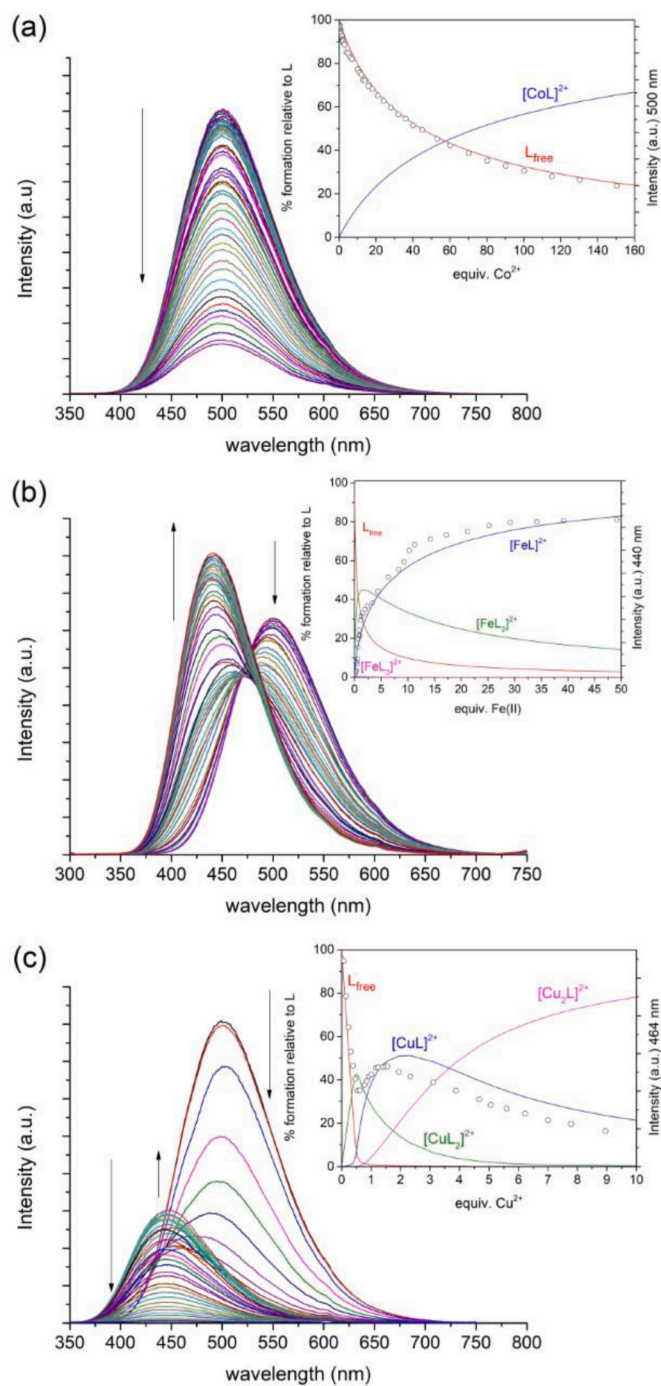The stoichiometry of the different [Fe:**L1**] species present in

equilibrium was also confirmed by mass spectrometry (Fig. S31), supporting the model used for the determination of the association constants.

In contrast, upon titration with Cu^{2+} spectral blue-shift of the emission band is also detected, although with lower emission of the resulting species, and with a concomitant dramatic quenching effect along with successive increase in Cu^{2+} (Fig. 6c). These discriminating optical responses "turn-on-blue-shift" emission upon coordination for

Fe²⁺ and Cu²⁺ followed by a total loss of fluorescence in the case of Cu²⁺, endow **L1** with bi-stimuli-channel sensing nature for both metal ions. The high resolution mass spectra recorded for solutions of **L1** in the presence of 0.5 and 1 equivalents of Cu(ClO₄)₂ show peaks due to 1:1 and 1:2 [Cu:**L1**] species (Fig. S32). Afterwards, we also investigated the sensing ability of **L1** towards other mono- and divalent cations. The addition of Na⁺, Mg²⁺, Hg²⁺ or Ag⁺ ions does not induce any significant change in the emission spectra (Figs. S23–S29), indicating the lack of affinity between the ligand and these metal ions.

2.5.3. Stability constants with cations

The results obtained for the binding constants from spectrophotometric titrations using HypSpec software, [26] through the non-linear least squares fit of the data which are summarized in Table 2. The best fitting of the titration profiles corresponds to a process with a 1:1 stoichiometry for Mn²⁺, Zn²⁺ and Co²⁺, whereas for Ni²⁺ and Fe²⁺, the presence of three stepwise equilibria were examined (log K_{11}, log K_{12} and log K_{13}). In the case of Cu²⁺, to determine the association constants, a 2:1 [Cu:**L1**] species were also considered, obtaining the stepwise equilibrium constants (log K_{11}, log K_{12} and log K_{21}). The logarithms of the association constants for the formation of 1:1 complexes are in the 3.60–7.44 range. By way of comparison, **L1** formed, in general weaker complexes with values of the logarithms of the stability constants of 3.60, 3.96, 4.34 and 3.94 for the coordination with Mn²⁺, Co²⁺, Ni²⁺ and Zn²⁺ respectively, although these values are within the range of those previously reported. [27] Regarding the values obtained for Fe²⁺ (6.71) and Cu²⁺ (7.44) ions, indicated a strong interaction compared with other 3*d* divalent metal ions of this study and also with other chemosensors previously reported for Fe²⁺ [28] and Cu²⁺ [8b,29].

2.5.4. Detection limit (LOD)

Futhermore, the detection limit (LOD) for the studied metal ions was calculated on the basis of the fluorescence titration using the formula 3σ/m where σ represents the standard deviation of a blank signal and m represents the slope of the ratio of emission intensity *versus* increased equivalents of the metal ion (Figs. S33–S38 and Tables S4 and S5). It is of interest to note that the LOD values obtained are in agreement with the association constant trend previously determined. The Cu²⁺ metal ion shows the more promising result having the lowest LOD (2.76·10⁻⁸ M). Such a low detection limit is significantly improved by one to two orders of magnitude, in comparison to other previously reported fluorescent chemosensors (Table S6). Finally, the limit of quantification (QL) of **L1** towards Cu²⁺ was also calculated by using the formula 10σ/*m*. [30] In this work, QL was calculated as 0.092 μM which reveals a great sensitivity of chemosensor towards Cu²⁺.

2.6. Density functional theory calculations

In order to understand the different optical responses that were observed for **L1** towards the selected metal ions, DFT calculations were performed for both ligands in CH₃CN using the polarizable continuum model (PCM). The minimized geometry of Zn(**L1**)(H₂O)₄ obtained by DFT calculations (TPSSh/Def2-TZVPP) (Fig. S39) shows an almost

planar conformation, where one of the methoxyphenyl groups, the imidazole ring and the triazole-trifluorophenyl moiety are practically in the same plane, as previously observed in the solid state crystal structure of the ligand **L2** in its protonated form. In addition, the DFT optimized geometries obtained for Zn(**L1**)Cl₂ and Zn(**L1**)(H₂O)₄ complexes present structural similarities (Fig. S39). In both cases, the ligand is coordinated to the metal ion in a bidentate chelating mode, adopting a *syn* conformation as observed in the crystal structure of [Zn(**L2**)Cl₂]. In the case of Zn(**L1**)Cl₂, the coordination polyhedron can be described as a flattened distorted tetrahedron, whereas for Zn(**L1**)(H₂O)₄, it is best described as a distorted octahedron, according to its higher coordination number. As a result of the different environment around the metal ion, the planarity of the ligand is compromised due to distinct steric hindrance, inducing the rotation of the methoxyphenyl group anchored to C(4') of the imidazole ring with respect to the conformation in the free ligand. Thus, the value of the dihedral angle that relates both aromatic rings increases from 24.0° in **L1** to 38.3° in Zn(**L1**)Cl₂ and 49.1° in Zn(**L1**)(H₂O)₄, reflecting a clear loss of planarity in the ligand backbone upon coordination of the Zn²⁺ that may disfavour the ICT transition and modify the optical response of the fluorophore.

The analysis of frontier molecular orbitals shows that for both ligands the HOMOs primarily reside on the 4-methoxyphenyl or 4-(*N,N*-dimethylamino)phenyl imidazole backbones, whereas the LUMOs are located on the triazole-(4-trifluoromethyl)phenyl core (Fig. 7b and S40). The inspection of the frontier molecular orbitals also shows that both HOMO and LUMO have considerable density on the imidazole ring, allowing the necessary overlap between electron-donor and electron-acceptor groups that facilitates the internal charge transfer process.

The electronic absorption spectra were calculated with TDDFT for **L1**, Zn(**L1**)Cl₂ and Zn(**L1**)(H₂O)₄ systems. As showed in Fig. 7a, a good agreement is observed between the computed absorption wavelengths and the experimental bands with discrepancies below 10 nm (Fig. S41 for **L2**). The lowest singlet state S₁, with an oscillator strength of 0.4903, corresponds to the ICT transition that implies both HOMO and LUMO orbitals, confirming the shift of the electron density from the electron donor group to the acceptor moiety upon photoexcitation (Fig. 7b). The next singlet states S₂ and S₃ are energetically close to S₁, at 0.37 eV and 0.44 eV, respectively. Both states are located on the electron-donor groups of the ligand, and while S₂ possesses no appreciable oscillator strength (0.0517), the S₃ state presents a higher value of around 0.5357 eV. Finally, the S₄ and S₅ states with oscillator strengths of 0.4156 and 0.1782, are more energetically separated from S₁ but also located on the electron-donor groups, being responsible of the high energy band observed in the measured spectrum (Table S7).

The modified optical response observed for the fluorophore upon coordination with Zn²⁺ that disfavours the ICT transition due to loss of planarity, also provokes other striking effects when analysing the calculated electronic transitions in both systems. Interestingly, upon coordination of Zn²⁺, the energy difference between the singlet states S₁ and S₂ decreases (Fig. 8), which could favour a potential intercrossing of both states. [31] This situation could explain the non-radiative deactivation observed when coordinating several metal ions such as Co²⁺, Ni²⁺ or Zn²⁺. The coordination of the metal ion blocks the ICT transition by rotating the electron-donor unit of the receptor, and the relative stabilization of the singlet state S₂ respect to S₁ may deactivate the emission through a non-emissive pathway (Fig. 8a), provoking the quenching of the initial fluorescence of the ligand. On the other hand, and depending on the nature of the coordinated metal ion (Mn²⁺ or Fe²⁺), although the ICT should be also blocked upon coordination, the relative stabilization of the singlet state S₂ could not be enough to cross S₁, resulting in a LC fluorescence that is blue-shifted with respect to the emission observed for the free ligand (Fig. 8c). In the case of Cu²⁺, a similar behaviour could be assumed, although it cannot be ruled out that the different emission pattern may also arise from a LMCT excited state.

We have performed this study using perchlorate as counterion, in order to analyse only the optical response of the system against different

Table 2

Association constants (log K values) and p*M* values obtained from spectrophotometric titrations in CH₃CN solution of **L1** with selected metal salts.

	Mn²⁺	Fe²⁺	Co²⁺	Ni²⁺	Cu²⁺	Zn²⁺
log K_{11}	3.60(1)	6.71(2)	3.96(1)	4.34(1)	7.44(2)	3.94(1)
log K_{12}	–	7.13(3)	–	5.90(1)	7.54(2)	–
log K_{13}	–	4.16(5)	–	4.56[b]	–	–
log K_{21}	–	–	–	–	5.54 (1)	–
p*M*[a]	6.01	6.58	6.03	6.59	11.26	6.03

[a] p*M* values defined as p*M* = −log[M²⁺]_free, with [M²⁺] = 10⁻⁶ M and [**L1**] = 10⁻⁵ M.
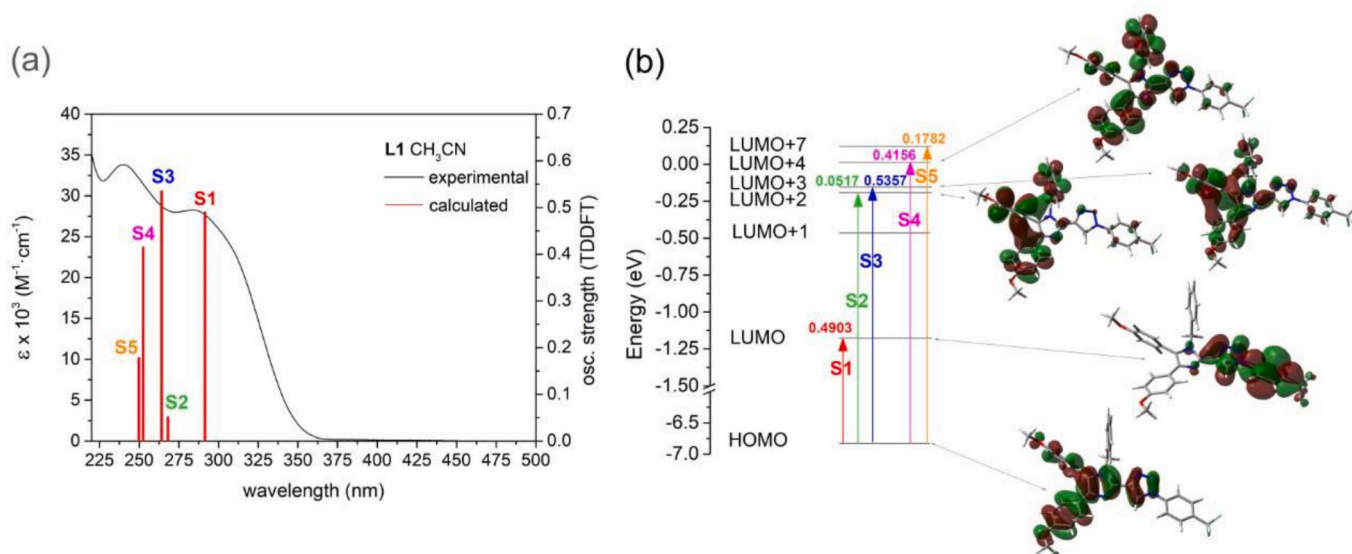
[b] Fixed during the fitting.

Fig. 7. (a) Absorption bands calculated at the PCM/M08HX/Def2-TZVPP level, compared with the experimental spectrum of **L1** measured in CH$_3$CN. (b) Calculated electronic transitions and involved molecular orbitals from optimization geometry in the free ligand **L1**. Absorption bands calculated of **L2** (Figs. S41 and SI).
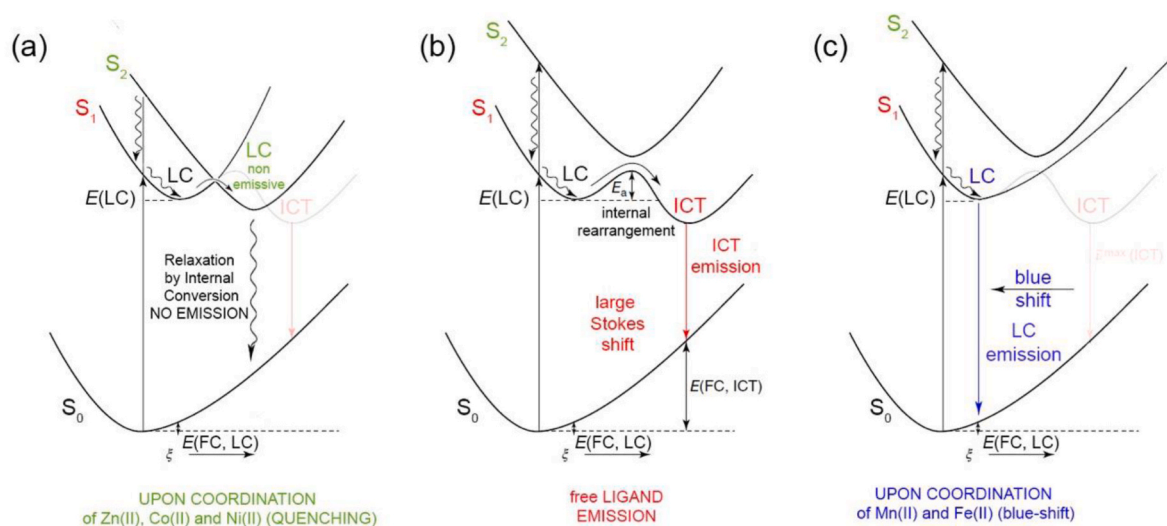

Fig. 8. Schematic representation of the possible radiative (pathway a) or non-radiative (pathway c) deactivation of the fluorophore through different mechanisms upon coordination, depending on the nature of the metal ion.

divalent metal ions. However, the optical properties of the ligand and its spectrofluorometric behaviour when interacting with different substrates, may be useful for the design of both cationic, anionic or combined sensors. Hydrogen bond interactions or the incorporation of different anions into coordination sphere of a selected metal ion may also modulate the optical response of the system. Thus, the effect of the counterion could be also decisive and give rise to new and unexpected optical responses that may be used as logic operations when designing multiply configurable boolean or fuzzy logic systems based on the optical output of the fluorophore. [32]

3. Conclusions

In this article, two novel *push-pull* imidazole-triazole based ligands **L1** and **L2** were designed and efficiently synthetized through Pd-catalyzed cross-coupling reactions with triorganoindium reagents and CuAAC as key steps. Their photophysical properties are strongly affected by the nature of the electron-donating group at C(4') and C(5') positions

of imidazole moiety. Both compounds displayed absorption wavelengths in the UV or visible region, emission in the visible region with large Stokes shifts and strong emission solvatochromism which support the formation of a very polar excited ICT. During the titration, the 1,2,3-triazole ring suffers and a rearrangement rotating 180° with respect to the imidazole core around the C(4)$_{triaz}$-C(2')$_{imid}$ bond. This feature endows **L1** to act in a bidentate chelating mode, accurately confirmed by X-ray spectroscopic studies. The **L1** complexing with various metal ions studied through fluorescence spectroscopy showed its selectivity towards Fe^{2+} and Cu^{2+} ions with stronger binding affinity by two distinct fluorescence responses, offering the lowest detection limit with Cu^{2+} (2.76·10^{-8} M). Titration studies and binding mechanisms proposed on the basis of DFT calculations revealed that Co^{2+}, Ni^{2+} and Zn^{2+} induced rotation of the electron-donor unit of the receptor and therefore the ICT transition is blocked provoking the quenching of the fluorescence emission. However, with Fe^{2+} and Mn^{2+} an unusual LC fluorescence that is blue-shifted with respect to the emission observed for the free ligand takes place. Upon titration with Cu^{2+} a similar spectral blue-shift is

observed but in this case accompanied as well by a dramatic quenching effect which may also arise from a LMCT excited state. Further research will focus on exploring the optical response in the presence of different anions and its potential applications in biological or environmental chemistry' as a solvatochromic probes.

4. Experimental section

4.1. General methods

All reactions were carried out in flame-dried glassware, under argon atmosphere, using standard gas-tight syringes, cannulae and septa. Tetrahydrofuran (THF) was dried by distillation from sodium/benzophenone. Reaction temperatures refer to external bath temperatures. Butyllithium (2.5 M in hexane) and 4-methoxyphenylmagnesium (0.5 M in THF) were titrated prior to use. [33] The solution of $InCl_3$ (0.45 M in THF) was prepared from commercial indium trichloride (99.99%). Triorganoindium compounds were prepared according to previously published methods [34] by treatment of the corresponding organolithium or Grignard reagent (3.0 equiv., ~0.5 M in dry THF) with a solution of $InCl_3$ (1.0 equiv., ~0.45 M in dry THF) at −78 °C and warming to room temperature and were used without isolation. 4-Bromo-*N,N*-dimethylaniline was lithiated by treatment with *n*-BuLi (1 equiv) at −78 °C in dry THF. $Pd(PPh_3)_4$ was prepared according the stablished method. [35] All other commercially available reagents were used as received. Organic extracts were dried over anhydrous $MgSO_4$, filtered and concentrated using a rotary evaporator at aspirator pressure. Reactions were monitored by TLC using pre-coated silica gel plates (0.20 mm thick), UV light as the visualizing agent and ethanolic phosphomolybdic acid as the developing agent. Flash column chromatography was performed with 230–400 mesh silica gel packed in glass columns. [36] ^1H and ^{13}C NMR spectra were recorded in $CDCl_3$ at 300 MHz for ^1H and 75 MHz for ^{13}C, at room temperature, and calibrated to the solvent peak. DEPT data were used to assign carbon types. Chemical shifts are reported in ppm (δ) relative to the solvent. The low and high resolution mass spectra were measured on a MAT95XP Magnetic Sector-EI spectrometer or with a QSTAR Elite hybrid quadrupole time-of-flight (TOF) ESI mass spectrometer, both operating in positive ionization mode. The IR spectra were taken with ATR ("attenuated total reflectance"). HPLC analyses were performed by using a Silica column (250 × 10 mm). Melting points are uncorrected.

4.2. Physical measurements

Ultraviolet/Visible (UV/Vis) absorption and fluorescence spectra were recorded with standard 1 cm quartz cells. Emission spectra were recorded using a spectrofluorometer equipped with a pulsed xenon flash-lamp as a light source. Compounds were excited at their excitation maxima (band of lowest energy) to record the emission spectra. The concentration of the compound solutions (in $CHCl_3$) was adjusted to $2.0 \cdot 10^{-6}$ M. Fluorescence quantum yields (Φ_F) values were determined by comparison with quinine sulfate in H_2SO_4 0.1 M as reference ($\Phi_F = 0.55$, H_2SO_4 0.1 M). [37] Stokes shifts were calculated by considering the lowest energetic absorption band. Molar absorptivity and fluorescence quantum yield were calculated as shown in the spectroscopic measurements (Supplementary Material). Stock solutions of the all cations: $Cu(ClO_4)_2 \cdot 6H_2O$, $CoCl_2$, $Mg(ClO_4)_2$, $Fe(ClO_4)_2 \cdot 6H_2O$, Ni $(ClO_4)_2 \cdot 6H_2O$, $Mn(ClO_4)_2 \cdot 6H_2O$, $ZnCl_2$, $NaClO_4$, $Mg(ClO_4)_2$, $HgCl_2$ and $AgClO_4$ were prepared at 10^{-3} M in CH_3CN. The UV–Vis and fluorescence titrations were measured at room temperature. During the titration, different amounts of metal salts were added by microsyringe to a solution of **L1** ($2.0 \cdot 10^{-6}$ M), maintaining the total concentration of the ligand constant by adding the same amounts of a solution of **L1** ($4.0 \cdot 10^{-6}$ M) in each case. The binding constants were calculated by Hyperquad software. The detection limit (LOD) was determined from the fluorescence titration data based on a reported method. [38]

4.3. Crystal structural determination

Suitable crystals of [(H**L2**)·ClO_4] (CCDC 2094919) and [Zn(L2)(Cl_2)] (CCDC 2094920) were analysed at 100 K using a Bruker D8 Venture diffractometer with a Photon 100 CMOS detector and Mo-Kα radiation ($\lambda = 0.71073$ Å) generated by an Incoatec high brillance microfocus source equipped with Incoatec Helios multilayer optics. APEX3 [39] was used for collecting frames of data, indexing reflections, and the determination of lattice parameters. Integration of intensity was made with SAINT. [40] Empirical absorption correction was carried out with SADABS. [41] The structure was solved with SHELXT. [42] The refinements were carried out by using full-matrix least-squares techniques on F^2 using the program SHELXL-2014. [43] Hydrogen atoms were calculated. Highly disordered solvent molecules were removed from the electron density map of [Zn(L)(Cl_2)] using the OLEX [44] solvent mask command. Drawings were produced with OLEX.

4.4. Computational details

Full geometry optimization of the free ligands and both Zn(II) complexes were performed with the Gaussian16 program package, [45] using the hybrid *meta*-GGA TPSSh [46] exchange-correlation functional and the Def2-TZVPP [47] basis set. Bulk solvent effects were incorporated in all calculations using the polarized continuum model with the default settings implemented in G16. [48] The size of the integration grid was increased with the integral = superfinegrid keyword. The nature of the energy minima for the optimized geometries was confirmed by the corresponding frequency analysis. Theoretical absorption spectra of **L1**, **L2** and Zn(II) complexes derived from **L1** were calculated using the M08HX exchange correlation functional from the Minnesota family that was found to be particularly well suited to compute electronic absorption spectra in systems that present CT transitions. [49] Time-dependent density functional theory (TDDFT) [50] was used to calculate the 10 lowest energy singlet-singlet transitions. Views of the structures and MOs were generated using the GaussView 6.0 program.

4.5. Synthesis

4.5.1. Benzyl-4,5-diiodo-2-((trimethylsilyl)ethynyl)-1H-imidazole (2)
A solution of tris[(trimethylsilyl)ethynyl]indium (5.0 mL, 0.261 mmol) was added to a solution of 1-benzyl-2,4,5-triiodo-1*H*-imidazole [51] (350.2 mg, 0.653 mmol) and $Pd(PPh_3)_4$ (45.5 mg, 0.039 mmol) in dry THF (3.3 mL) in a Schlenk tube filled with argon. The reaction mixture was heated at 80 °C until the starting material was consumed (20 h). The mixture was cooled to room temperature and quenched by the addition of a few drops of MeOH. The solvent was evaporated under reduced pressure and the residue was diluted with EtOAc (25 mL). The organic phase was washed with brine (2 x 10 mL), dried, and concentrated. The residue was purified by flash column chromatography (30% EtOAc/hexanes) to afford, after concentration and high-vacuum drying, compound **2** as a yellow oil (190 mg, 57%). ^1H NMR ($CDCl_3$, 300 MHz): 7.30–7.34 (m, 3H), 7.21–7.24 (m, 2H), 5.30 (s, 2H), 0.20 (s, 9H); ^{13}C {1H} NMR ($CDCl_3$, 75 MHz): 136.1 (C), 135.0 (2 x C), 128.8 (2 x CH), 128.3 (CH), 127.6 (2 x CH), 102.3 (C), 96.4 (C), 92.3 (C), 52.9 (CH_2), −0.5 (3 x CH_3); IR (ATR) ν = 2958, 1597, 1462, 1381, 1250, 842 cm^{-1}; MS (EI) *m/z* (%) 506 [M]$^+$ (74); HRMS (EI-ion trap): calcd for $C_{15}H_{16}I_2N_2Si$ [*m/z*], 505.9167 [M]$^+$; found, 505.9162.

4.5.2. 1-Benzyl-4,5-bis(4-methoxyphenyl)-2-((trimethylsilyl)ethynyl)-1H-imidazole (3a)
A solution of the tri(4-methoxyphenyl)indium (9.0 mL, 0.375 mmol) was added to a THF solution of 1-benzyl-4,5-diiodo-2-((trimethylsilyl) ethynyl)-1*H*-imidazole (190 mg, 0.375 mmol) and $Pd(PPh_3)_4$ (22.1 mg, 0.019 mmol) in dry THF (2.0 mL) in a Schlenk tube filled with argon. The resulting mixture was heated at 80 °C until the starting material was consumed (21 h), cooled to room temperature and quenched by the

addition of a few drops of MeOH. The solvent was evaporated under reduced pressure and the residue was diluted with EtOAc (25 mL). The organic phase was washed with brine (2 x 10 mL), dried, and concentrated. The residue was purified by flash column chromatography (50% EtOAc/hexanes) to afford, after concentration and high-vacuum drying compound **3a** (109 mg, 63%) as a yellow solid. Mp = 129–131 °C. ^{1}H NMR (CDCl$_3$, 300 MHz): 7.43 (dt, $J = 8.9$, 2.3 Hz, 2H), 7.22–7.26 (m, 3H), 7.05 (dt, $J = 8.7$, 2.2 Hz, 2H), 6.95–6.97 (m, 2H), 6.88 (dt, $J = 8.9$, 2.3 Hz, 2H), 6.74 (dt, $J = 8.9$, 2.5 Hz, 2H), 5.08 (s, 2H), 3.83 (s, 3H), 3.74 (s, 3H), 0.19 (s, 9H); ^{13}C{1H} NMR (CDCl$_3$, 75 MHz): 160.0 (C), 158.4 (C), 138.4 (C), 136.8 (C), 132.2 (2 x CH), 131.2 (C), 128.8 (C), 128.5 (2 x CH), 128.0 (2 x CH), 127.6 (CH), 127.1 (2 x CH), 126.7 (C), 122.4 (C), 114.4 (2 x CH), 113.5 (2 x CH), 100.1 (C), 94.2 (C), 55.3 (CH$_3$), 55.1 (CH$_3$), 48.5 (CH$_2$), −0.4 (3 x CH$_3$); IR (ATR) ν = 3290, 2954, 2927, 2854, 2157, 1614, 1528, 1498, 1356 cm^{-1}; MS (EI) m/z (%) 466 [M]$^+$ (100); HRMS (EI-ion trap): calcd for C$_{29}$H$_{30}$N$_2$O$_2$Si [m/z], 466.2071 [M]$^+$; found, 466.2070.

Compound 3a can be prepared from 1 in a one-pot procedure. A solution of tris[(trimethylsilyl)ethynyl]indium reagent (8.5 mL, 0.448 mmol) was added to a solution of 1-benzyl-2,4,5-triiodo-1H-imidazole (401.2 mg, 0.746 mmol) and Pd(PPh$_3$)$_4$ (42.3 mg, 0.037 mmol in dry THF (3.7 mL) in a Schlenk tube filled with argon. The resulting mixture was heated at 80 °C until the starting material was consumed (20 h). Then, a solution of tri(4-methoxyphenyl)indium (20.3 mL, 1.12 mmol) was added and the mixture was heated at 80 °C for (21 h). The mixture was cooled to room temperature, quenched by the addition of a few drops of MeOH. The solvent was evaporated under reduced pressure and the residue was diluted with EtOAc (25 mL). The organic phase was washed with brine (2 x 10 mL), dried, and concentrated. The residue was purified by flash column chromatography (20% EtOAc/hexanes) to afford, after concentration and high-vacuum drying compound 3a as a yellow oil (107.4 mg, 31%, 2 steps).

4.5.3. 4,4'-(1-Benzyl-2-((trimethylsilyl)ethynyl)-1H-imidazole-4,5-diyl) bis(N,N-dimethyl-aniline) (3b)

A solution of the tris(4-N,N-dimethylaminophenyl)indium (13.5 mL, 0.73 mmol) was added to a THF solution of 1-benzyl-4,5-diiodo-2-((trimethylsilyl)ethynyl)-1H-imidazole (304.8 mg, 0.602 mmol) and Pd (PPh$_3$)$_4$ (36.3 mg, 0.031 mmol) in dry THF (3.0 mL) in dry THF (2.0 mL) in a Schlenk tube filled with argon. The resulting mixture was heated at 80 °C until the starting material was consumed (17 h), cooled to room temperature, quenched by the addition of a few drops of MeOH and the solvent was evaporated under reduced pressure. The solvent was evaporated under reduced pressure and the residue was diluted with EtOAc (25 mL). The organic phase was washed with brine (2 x 10 mL), dried, and concentrated. The residue was purified by flash column chromatography (30% EtOAc/hexanes 1:1) to afford, after concentration and high-vacuum drying compound **3b** (175 mg, 60%) as a yellow solid. Mp = 169–170 °C. ^{1}H NMR (CDCl$_3$, 300 MHz): 7.51 (dt, $J = 8.8$, 2.3 Hz, 2H), 7.24–7.29 (m, 3H), 7.04–7.07 (m, 4H), 6.70 (dt, $J = 8.8$, 2.2 Hz, 2H), 6.62 (dt, $J = 8.9$, 2.2 Hz, 2H), 5.12 (s, 2H), 3.03 (s, 6H), 2.91 (s, 6H), 0.23 (s, 9H); ^{13}C{1H} NMR (CDCl$_3$, 75 MHz): 150.7 (C), 149.5 (C), 138.9 (C), 137.6 (C), 132.1 (2 x CH), 130.9 (C), 129.5 (C), 128.7 (2 x CH), 127.8 (2 x CH), 127.7 (CH), 127.4 (2 x CH), 123.4 (C), 118.0 (C), 112.6 (2 x CH), 112.5 (2 x CH), 99.8 (C), 95.2 (C), 48.6 (CH$_2$), 40.9 (2 x CH$_3$), 40.6 (2 x CH$_3$), 0.0 (3 x CH$_3$); IR (AT R) ν = 3290, 2954, 2927, 2853, 2157, 1614, 1528, 1489, 1356 cm^{-1}; MS (EI) m/z (%) 492 [M]$^+$ (41); HRMS (EI-ion trap): calcd for C$_{31}$H$_{36}$N$_4$Si [m/z], 492.2704 [M]$^+$; found, 492.2705.

4.5.4. 1-Benzyl-4,5-bis(4-methoxyphenyl)-2-ethynyl-1H-imidazole (4a)

To a solution of 1-benzyl-4,5-*bis*(4-methoxyphenyl)-2-((trimethylsilyl)ethynyl)-1H-imidazole (67.1 mg, 0.143 mmol) and K$_2$CO$_3$ (25.3 mg, 0.172 mmol) in MeOH (6 mL) was added. The resulting mixture was stirred 20 min at room temperature. After completion the solvent was evaporated under reduced pressure and the residue was

purified by flash column chromatography (25% EtOAc/hexanes) to afford, after concentration and high-vacuum drying, compound **4a** as a yellow oil (51 mg, 89%). ^{1}H NMR (CDCl$_3$, 300 MHz): 7.45 (dt, $J = 8.9$, 2.3 Hz, 2H), 7.22–7.26 (m, 3H), 7.04 (dt, $J = 8.7$, 2.2 Hz, 2H), 6.93–6.96 (m, 2H), 6.87 (dt, $J = 8.9$, 2.3 Hz, 2H), 6.75 (dt, $J = 8.9$, 2.5 Hz, 2H), 5.11 (s, 2H), 3.82 (s, 3H), 3.74 (s, 3H), 3.35 (s, 1H); ^{13}C{1H} NMR (CDCl$_3$, 75 MHz): 160.0 (C), 158.5 (C), 138.6 (C), 136.6 (C), 132.2 (2 x CH), 130.3 (C), 129.0 (C), 128.6 (2 x CH), 127.9 (2 x CH), 127.6 (CH), 126.7 (2 x CH), 126.6 (C), 122.2 (C), 114.4 (2 x CH), 113.5 (2 x CH), 81.7 (CH), 73.9 (C), 55.3 (CH$_3$), 55.1 (CH$_3$), 48.4 (CH$_2$); IR (ATR) ν = 3282, 2956, 2926, 2839, 2046, 1604, 1518, 1495, 1455, 1248, 1174 cm^{-1}; MS (FAB) m/z (%) 395 [M]$^+$ (100); HRMS (FAB) calcd for C$_{26}$H$_{23}$N$_2$O$_2$ [m/z], 395.1754 [M]$^+$; found, 395.1736.

4.5.5. 1-Benzyl-4,5-bis-(4-N,N-dimethylaminophenyl)-2-ethynyl-1H-imidazole (4b)

To a solution of 1-benzyl-4,5-*bis*(4-N,N-dimethylaminophenyl)-2-((trimethylsilyl)-ethynyl)-1H-imidazole (160.1 mg, 0.325 mmol) and K$_2$CO$_3$ (54.1 mg, 0.390 mmol) in MeOH (6 mL) was added. The resulting mixture was stirred 20 min at room temperature. After completion the solvent was evaporated under reduced pressure and the residue was purified by flash column chromatography (30% EtOAc/hexanes) to afford, after concentration and high-vacuum drying, compound **4b** as a yellow solid (119 mg, 88%). ^{1}H NMR (CDCl$_3$, 300 MHz): 7.50 (dt, $J = 8.8$, 2.3 Hz, 2H), 7.26–7.28 (m, 3H), 7.01–7.03 (m, 4H), 6.67 (dt, $J = 8.8$, 2.2 Hz, 2H), 6.62 (dt, $J = 8.9$, 2.2 Hz, 2H), 5.13 (s, 2H), 3.34 (s, 1H), 3.00 (s, 6H), 2.91 (s, 6H); ^{13}C{1H} NMR (CDCl$_3$, 75 MHz): 150.8 (C), 149.6 (C), 139.2 (C), 137.5 (C), 132.1 (2 x CH), 130.1 (C), 129.6 (C), 128.8 (2 x CH), 127.8 (2 x CH), 127.7 (CH), 127.1 (2 x CH), 123.3 (C), 117.8 (C), 112.6 (4 x CH), 81.8 (CH), 74.7 (C), 48.5 (CH$_2$), 40.9 (2 x CH$_3$), 40.6 (2 x CH$_3$); IR (ATR) ν = 3280, 2922, 2853, 2805, 2112, 1613, 1527,6, 1498, 1443, 1353, 1217, 1193, 1168, 726 cm^{-1}; MS (EI) m/z (%) 420 [M]$^+$ (45); HRMS (EI-ion trap): calcd for C$_{28}$H$_{28}$N$_4$ [m/z], 420.2308 [M]$^+$; found, 420.2299.

4.5.6. 4-(1-Benzyl-4,5-bis(4-methoxyphenyl)-1H-imidazole-2-yl)-1-(4-(trifluoromethyl)-phenyl)-1H-1,2,3-triazole (L1)

A solution of 1-benzyl-4,5-*bis*(4-methoxyphenyl)-2-ethynyl-1H-imidazole (0.078 mg, 0.198 mmol), 1-azido-4-(trifluoromethyl)benzene (0.4 mL, 0.198 mmol), CuSO$_4$ (4.4 mg, 0.01 mmol) and sodium ascorbate (78.8 mg, 0.396 mmol) in MeOH/H$_2$O (2.4/1.6 mL) was stirred at room temperature until the starting material was consumed (1 h). After completion the reaction, the solution was poured into saturated aqueous NH$_4$Cl (20 mL) and extracted with CH$_2$Cl$_2$ (3 x 20 mL). The combined organic phase was washed with brine (20 mL), dried, filtered and concentrated. The residue was purified by flash column chromatography (20% EtOAc/hexanes) to afford, after concentration and high-vacuum drying, compound **L1** as a yellow solid (80.2 mg, 70%). HPLC (Silica column, 250 × 10 nm, solvent: 3.5–4.0% isopropanol in hexane, flow: 4.0 mL/min, $\lambda = 280$ nm): $t_R = 9.665$ min. Mp = 189–190 °C. ^{1}H NMR (CDCl$_3$, 300 MHz): 8.71 (s, 1H), 7.97 (d, $J = 7.9$ Hz, 2H), 7.84 (d, $J = 8.0$ Hz, 2H), 7.50 (dt, $J = 8.9$, 2.3 Hz, 2H), 7.14–7.20 (m, 5H), 6.89–6.94 (m, 4H), 6.79 (dt, $J = 8.9$, 2.5 Hz, 2H), 5.74 (s, 2H), 3.85 (s, 3H), 3.79 (s, 3H); ^{13}C{1H} NMR (CDCl$_3$, 75 MHz): 159.9 (C), 158.4 (C), 142.1 (C), 139.1 (C), 138.5 (C), 137.8 (C), 137.5 (C), 132.5 (2 x CH), 129.9 (C), 128.4 (2 x CH), 127.9 (2 x CH), 127.25 (C), 127.20 (CH), 127.15 (CH), 127.12 (CH), 127.06 (C), 126.4 (2 x CH), 125.3 (C), 122.4 (C), 120.9 (CH), 120.3 (2 x CH), 114.4 (2 x CH), 113.7 (2 x CH), 55.3 (CH$_3$), 55.2 (CH$_3$), 48.4 (CH$_2$); IR (ATR) ν = 3143, 3067, 3032, 3006, 2955, 2927, 2837, 1616, 1495, 1455, 1323, 1246, 1172, 1127, 1031, 837 cm^{-1}; MS (EI) m/z (%) 581 [M]$^+$ (100); HRMS (EI-ion trap): calcd for C$_{33}$H$_{26}$F$_3$N$_5$O$_2$ [m/z], 581.2033 [M]$^+$; found, 581.2029.

4.5.7. 4,4'-(1-Benzyl-2-(1-(4-(trifluoromethyl)phenyl)-1H-1,2,3-triazol-4-yl)-1H-imidazole-4,5-diyl)bis(N,N-dimethylaniline) (L2)

A solution of 1-benzyl-4,5-*bis*(4-N,N-dimethylaminophenyl)-2-

ethynyl-1*H*-imidazole (110.1 mg, 0.262 mmol), 1-azido-4-(trifluoro-methyl)benzene (0.52 mL, 0.262 mmol), $CuSO_4$ (4.5 mg, 0.013 mmol) and sodium ascorbate (104.9 mg, 0.524 mmol) in $MeOH/H_2O$ (4.8/3.2 mL) was stirred at room temperature until the starting material was consumed (1 h). After completion the reaction, the solution was poured into saturated aqueous NH_4Cl (20 mL) and extracted with CH_2Cl_2 (3 x 20 mL). The combined organic phase was washed with brine (20 mL), dried, filtered and concentrated. The residue was purified by flash column chromatography (20% EtOAc/hexanes) to afford, after concentration and high-vacuum drying, compound **L2** as a yellow solid (121 mg, 76%). HPLC (Silica column, 250 × 10 nm, solvent: 4.8–6.0% isopropanol in hexane, flow: 4.0 mL/min, $\lambda = 254$ nm): $t_R = 12.306$ min. Mp = 226–227 °C. ^{1}H NMR ($CDCl_3$, 300 MHz): 8.78 (s, 1H), 7.94 (d, $J = 8.5$ Hz, 2H), 7.79 (d, $J = 8.6$ Hz, 2H), 7.50 (dt, $J = 8.8$, 2.3 Hz, 2H), 7.15–7.19 (m, 3H), 7.10 (dt, $J = 8.8$, 2.2 Hz, 2H), 6.94–6.96 (m, 2H), 6.69 (dt, $J = 8.8$, 2.2 Hz, 2H), 6.64 (dt, $J = 8.9$, 2.2 Hz, 2H), 5.72 (s, 2H), 2.99 (s, 6H), 2.91 (s, 6H); ^{13}C{1H} NMR ($CDCl_3$, 75 MHz): 150.8 (C), 149.7 (C), 142.5 (C), 139.6 (C), 138.9 (C), 138.6 (C), 137.3 (C), 132.5 (2 x CH), 130.6 (C), 128.8 (2 x CH), 127.9 (2 x CH), 127.6 (CH), 127.58 (CH), 127.54 (C), 127.4 (CH), 126.8 (2 x CH), 125.4 (C), 123.4 (C), 121.4 (CH), 120.7 (2 x CH), 118.0 (C), 112.8 (2 x CH), 112.7 (2 x CH), 48.7 (CH_2), 41.0 (2 x CH_3), 40.7 (2 x CH_3); IR (ATR) $\nu = 3070$, 3032, 2887, 2854, 2800, 1614, 1525, 1502, 1443, 1322, 1122, 1110, 1065, 1028, 820 cm^{-1}; MS (EI) m/z (%) 607 $[M]^+$ (100); HRMS (EI-ion trap): calcd for $C_{35}H_{32}F_3N_7$ $[m/z]$, 607.2666 $[M]^+$; found, 607.2666.

CRediT authorship contribution statement

Ana Da Lama: Investigation, Methodology, Validation, Writing – original draft. **José Pérez Sestelo:** Conceptualization, Writing – review & editing. **Laura Valencia:** Investigation, (X-ray). **David Esteban-Gómez:** Conceptualization, Formal analysis, Supervision, Writing – original draft, Writing – review & editing. **Luis A. Sarandeses:** Conceptualization, Supervision, Writing – original draft, Writing – review & editing. **M. Montserrat Martínez:** Conceptualization, Supervision, Methodology, Project administration, Writing – original draft, Writing – review & editing.

Declaration of competing interest

The authors declare that they have no known competing financial interests or personal relationships that could have appeared to influence the work reported in this paper.

Data availability

Data will be made available on request.

Appendix A. Supplementary data

Supplementary data to this article can be found online at https://doi.org/10.1016/j.dyepig.2022.110539.

References

[1] (a) Fausto da Silva JJR, Williams RJP. In: The biological chemistry of the elements. second ed. New York: Oxford University; 2001, ISBN 9780198508489. (b) Tapiero H, Townsend DM, Tew KD. Trace elements in human physiology and pathology. Copper. Biomed Pharmacother 2003;57:386–98.(c) Kim HM, Cho BR. Two-photon probes for intracelular free metal ions, acidic vesicles, and lipid rafts in live tissues. Acc Chem Res 2009;42:863–72.

[2] Que EL, Domaille DW, Chang CJ. Metals in neurobiology: probing their chemistry and biology with molecular imaging. Chem Rev 2008;108:1517–49.

[3] (a) Crichton R, Boelaert JR. In: Genetics of iron storage and hemochromatosis in inorganic biochemsitry of iron metabolism: from molecular mechanism to clinical consequences. second ed. Wiley; 2002.(b) Barnham KJ, Masters CL, Bush AI. Neurodegenerative diseases and oxidative stress. Nat Rev Drug Discov 2004;3:205–14.

[4] (a) Gaggelli E, Kozlowski H, Valensin D, Valensin G. Copper homeostasis and neurodegenerative disorders (Alzheimer's, Prion, and Parkinson's diseases and Amyotrophic Lateral Sclerosis). Chem Rev 2006;106:1995–2044.(c) Bandmann O, Weiss KH, Kaler SG. Wilson's Disease and other neurological copper disorders. Lancet Neurol 2015;14:103–13.

[5] (a) Kowser Z, Rayhan U, Akther T, Redshaw C, Yamato T. A brief review on novel pyrene based fluometric and colorimetric chemosensors for the detection of Cu^{2+}. Mater Chem Front 2021;15:2173–200.(b) Wu D, Sedgwick AC, Gunnlaugsson T, Akkaya EU, Yoon J, James TD. Fluorescent chemosensors: the past, present and future. Chem Soc Rev 2017;46:7105–23.(c) Patil A, Salunke-Gawali S. Overview of the chemosensor ligands used for selective detection of anions and metal ions (Zn2+, Cu2+, Ni2+, Co2+, Fe2+, Hg2+). Inorg Chim Acta 2018;482:99–112.(d) Hirayama T. Fluorescent probes for the detection of catalytic Fe(II) ion. Free Radic Biol Med 2019;133:38–45.(e) Shyamsivappan S, Saravanan A, Vandana N, Suresh T, Suresh S, Nandhakumar R, et al. Novel quinoline-based thiazole derivatives for selective detection of Fe^{3+}, Fe^{2+}, and Cu^{2+} ions. ACS Omega 2020;5:27245–53.(f) Lu Y, Ruan G, Du W, Li J, Yang N, Wu Q, et al. Recent progress in rational design of fluorescent probes for Fe^{2+} and bioapplication. Dyes Pigments 2021;190:109337.(g) Mansha A, Asad SA, Asim S, Bibi S, Rehman S-U, Shahzad A. Review of recent advancements in fluorescent chemosensor for ion detection via coumarin derivatives. Chem Pap 2022. https://doi.org/10.1007/s11696-022-02092-5.(h) Topa-Skwarczyńska M, Szymaszek P, Fiedor P, Chachaj-Brekiesz A, Galek M, Kasprzk W. Pyridine derivatives as candidates for selective and sensitive fluorescent biosensors for lung cancer cell imaging and iron ions detection. Dyes Pigments 2022;200:110171.

[6] Ferreira RCM, Raposo MMM, Costa SPG. Novel alanines bearing a heteroaromatic side chain: synthesis and studies on fluorescent chemosensing of metal cations with biological relevance. Amino Acids 2018;50. 671–84.

[7] (a) Daly B, Ling J, Prasanna de Silva A. Current developments in fluorescent PET (Photoinduced Electron Transfer) sensors and switches. Chem Soc Rev 2015;44:4203–11.(b) Gao M, Tang BZ. Fluorescent sensors based on aggregation-induced emission: Recent advances and perspectives. ACS Sens 2017;2:1382–99.(c) Wu L, Huang C, Emery BP, Sedgwick AC, Bull SD, He X-P, et al. Förster resonance energy transfer (FRET)-based small-molecule sensors and imaging agents. Chem Soc Rev 2020;49:5110–39.

[8] (a) Wang Y, Zhou J, Zhao L, Xu B. A Dual-responsive and highly sensitive fluorescent probe for Cu^{2+} and pH based on a dansyl derivative. Dyes Pigments 2020;180:108513.(b) Savithri K, Prabhakaran R, Paulpandi M, Enoch IVMV, Mohan PS. An Anticancer active imidazole analogue as a fluorescent sensor: Sensitive and selective detection of Cu^{2+} ions. Transit Met Chem 2020;45:443–5.

[9] Montalti M, Washwa S, Kim WY, Kipp RA, Schmehl RH. Luminiscent ruthenium(II) bipyridyl-phosphonic acid complexes: pH dependent photophysical behaviour and quenching with divalent metal ions. Inorg Chem 2000;39:76–84.

[10] (a) Li Z, Zhang L, Wang L, Guo Y, Cai L, Yu M, et al. Highly sensitive and selective fluorescent sensor for Zn^{2+}/Cu^{2+} and new approach for sensing Cu^{2+} by central metal displacement. Chem Commun (J Chem Soc Sect D) 2011;47:5798–800.(b) Bhaumik C, Das S, Maity D, Baitalik SA. Terpyridyl-imidazole (Tpy-HImzPh3) based bifunctional receptor for multichannel detection of Fe2+ and F− ions. Dalton Trans 2011;40. 11795–808.(c) Bhaumik C, Maity D, Das S, Baitalik S. Synthesis, structural characterization, solvatochroism, and ion-binding studies of a ditopic receptor based on 2-(4-[2,2':6',2''] terpyridin-4'-ylphenyl)-1H-phenantro [9,10-d]imidazole (tpy-HImzphen) unit. RSC Adv 2012;2:2581–5800.(d) Kaur N, Alreja P. An imidazole based probe for relay recognition of Cu2+ and OH- ions leading to AND logic gate. J Chem Sci 2015;127:1253–9.(e) Yin H, Zhao B, Kan W, Liu T, Wang W, Yin G, et al. Hydroxyl phenyl imino modified phenantro[9,10-*d*] imidzole: An AIEE-active sensor for determination of Cu^{2+} in water samples and subsequent "turn-on" recognition of Cr^{3+} with logic gates. Spectrochim Acta Mol Biomol Spectrosc 2019;217:18–1259.

[11] Selvan GT, Varadaraju C, Selvan RT, Enoch IVMV, Selvakumar PM. On/off fluorescent chemosensor for selective detection of divalent iron and copper ions: Molecular logic operation and protein binding. ACS Omega 2018;3:7985–92.

[12] (a) Molina P, Tárraga A, Otón F. Imidazole Derivatives: A comprehensive survey of their recognition properties. Org Biomol Chem 2012;10:1711–24.

[13] (a) Eseola AO, Li W, Gao R, Zhang M, Hao X, Liang T, et al. Syntheses, structures, and fluorescent properties of 2-(1*H*-imidazole-2-yl)phenols and their neutral Zn(II) complexes. Inorg Chem 2009;48:9133–46.(b) Satapathy R, Wu Y-H, Lin H-C. Novel Thieno-imidazole based probe for colorimetric detection of Hg^{2+} and fluorescence turn-on response of Zn^{2+}. Org Lett 2012;14. 2564–7.(c) Das S, Karmakar S, Mardanya S, Baitalik S. Synthesis, structural characteriztion, and multichannel anion and cation sensing studies of a bifunctional Ru(II) polypyridyl–imidazole based receptor. Dalton Trans 2014;43:3767–9146.(d) Mardanya S, Karmakar S, Das S, Baitalik S. Anion and cation triggered modulation of optical properties of a pyridyl-imidazole receptor rigidly linked to pyrene and construction of INHIBIT, OR and XOR molecular logic gates: A combined experimental and DFT/TD-DFT investigation. Sens Actuators, B 2015;206. 701–13.(e) Alfonso M, Ferao AE, Tárraga A, Molina P. Electrochemical and fluorescent ferrocene-imidazole-based dyads as ion-pair receptors for divalent metal cations

and oxoanions. Inorg Chem 2015;54. 7461–73.(f) Alfonso M, Tárraga A, Molina P. Preparation and sensing properties of a nitrogen-rich ferrocene-imidazole-quinoxaline triad decorated with pyrrole rings. Dalton Trans 2016;45. 19269–76. (g) Cheng D, Liu X, Yang H, Zhang T, Han A, Zang LA. Cu^{2+}-Selective probe based on phenanthro-imidazole Derivative. Sensors 2017;17:35.(h) Alreja P, Kaur N. Modulation in photophysical properties of fluorescent imidazole possessing 1,10-phenantroline on introduction of Ru(bipy)22+ towards cation sensing. ChemistrySelect 2017;2:8638–9146.(i) Esteves CIC, Ferreira RCM, Raposo MMM, Costa SPG. New Fluoroionophores for metal cations based on benzo[*d*]oxazol-5-yl-alanine bearing pyrrole and imidazole. Dyes Pigments 2018;151:211–8.(j) Prabakaran G, Velmurugan K, Vickram R, David I, Thamilselvan A, Prabhu J, et al. Triphenyl-imidazole based reversible color/fluorimetric sensing and electrochemical removal of Cu2+ ions using capacitive deionization and molecular logic gates. Spectrochim Acta Mol Biomol Spectrosc 2021;246:119018.

[14] (a) Rostovtsev VV, Green LG, Fokin VV, Sharpless KB. A Stepwise Huisgen cycloaddition process: Copper(I)-catalyzed regioselective "ligation" of azides and terminal alkynes. Angew Chem Int Ed 2002;41:2596–9.(b) Haldón E, Nicasio MC, Pérez PJ. Copper-catalysed azide-alkyne cycloadditions (CuAAC): An update. Org Biomol Chem 2015;13. 9528–2599.

[15] (a) Lau YH, Rutledge PJ, Watkinson M, Todd MH. Chemical sensors that incorporate click-derived triazoles. Chem Soc Rev 2011;40:2848–66.(b) Schulze B, Schubert US. Beyond click chemistry – supramolecular interactions of 1,2,3-triazoles. Chem Soc Rev 2014;43:2522–866.(c) Ahmed F, Xiong H. Recent developments in 1,2,3-triazole-based chemosensors. Dyes Pigments 2021;185: 108905.

[16] Brombosz SM, Appleton AL, Zappas AJ, Bunz UHF. Water-soluble benzo and naphto-thiadiazole-based bistriazoles and their metal-binding properties. Chem Commun 2010;46:1419–21.(e) Molina P, Tárraga A, Alfonso M. Ferrocene-based multichannel ion-pair recognition receptors. Dalton Trans 2013;43:18–29.

[17] Lai Q, Liu Q, He Y, Zhao K, Wei C, Wojtas L, et al. Triazole-imidazole (TA-IM) derivatives as ultrafast fluorescent probes for selective Ag$^+$ detection. Org Biomol Chem 2018;16:7801–5.

[18] (a) Rossi R, Angelici G, Casotti G, Manzini C, Lessi M. Catalytic synthesis of 1,2,4,5-tetrasubstituted 1*H*-imidazole derivatives: State of the art. Adv Synth Catal 2019;361:2737–803.(b) Shabalin DA, Camp JE. Recent Advances in the synthesis of imidazoles. Org Biomol Chem 2020;18. 3950–2803.

[19] Koubachi J, Kazzouli SE, Bousmina M, Guillaumet G. Functionalization of imidazo [1,2-a]pyridines by means of metal-catalyzed cross-coupling reactions. Eur J Org Chem 2014;2014(24):5119–38.

[20] Pérez-Caaveiro C, Pérez Sestelo J, Martínez MM, Sarandeses LA. Triorganoindium reagents in selective palladium-catalyzed cross-coupling with iodoimidazoles: Synthesis of Neurodazine. J Org Chem 2014;79:9586–93.

[21] (a) Martínez MM, Peña-López M, Pérez Sestelo J, Sarandeses LA. Synthesis of functionalized thiophenes and oligothiophenes by selective and iterative cross-coupling reactions using indium organometallics. Org Biomol Chem 2012;10. 3892–8.
Pérez-Caaveiro C, Oliva MM, López Navarrete JT. Pérez Sestelo J, Martínez MM, Sarandeses LA. Synthesis of D–A–A and D–A–D pyrimidine π-systems using triorganoindium reagents: Optical, vibrational, and electrochemical studies. J Org Chem 2019;84:8870–85.

[22] Grabowski ZR, Rotkiewicz K, Rettig W. Structural changes accompanying intramolecular electron transfer: Focus on twisted intramolecular charge-transfer states and structures. Chem Rev 2003;103:3899–4032.

[23] (a) Atkins P, Friedman R. In: Molecular quantum mechanics. fifth ed. Oxford: Oxford University Press; 2011.(b) Coolidge AS, James HM, Present RD. A Study of the Franck-Condon principle. J Chem Phys 1936;4:193–211.(c) Bässler H, Schweitzer B. Site-selective fluorescence spectroscopy of conjugated polymers and oligomers. Acc Chem Res 1999;32:173–82.

[24] (a) Ning Z, Zhang Q, Wu W, Pei H, Liu B, Tian H. Starburst triarylamine based dyes for efficient dye-sensitized solar cells. J Org Chem 2008;73:3791–7.(b) Fischer MKR, Wenger S, Wang M, Mishra A, Zakeeruddin SM, Grätzel M, et al. D-π-A sensitizers for dye-sensitized solar cells: Linear *vs* branched oligothiophenes. Chem Mater 2010;22. 1836–45.(c) Tan Y, Liang M, Lu Z, Zheng Y, Tong X, Sun Z, et al. Novel triphenylamine donors with carbazole moieties for organic sensitizers toward cobalt(II/III) redox mediators. Org Lett 2014;16:3978–81.

[25] Das S, karmakar S, Mardanya S, Baitalik S. Synthesis, structural characterization, and multichannel anion and cation sensing studies of a bifunctional Ru(II) polypyridyl imidazole based receptor. Dalton Trans 2014;43:5767–82.

[26] Gans P, Sabatini A, Vacca A. Investigation of equilibria in solution. Determination of equilibrium constants with the HYPERQUAD suite of programs. Talanta 1996; 43:1739–53.

[27] (a) Gruppi F, Liang J, Bartelle BB, Royzen M, Turnbull DH, Canary JW. Supramolecular metal displacement allows on-fluorescence analysis of manganese (II) in living cells. Chem Commun 2012;48:10778–80.(b) Weerasinghe AJ, Oyeamalu AN, Abebe FA, Venter AR, Sinn E. Rhodamine based turn-on sensors for Ni^{2+} and Cr^{3+} in organic media: Detecting CN$^-$ via the metal displacement approach. J Fluoresc 2016;26:891–8.(c) Annaraj B, Mitu L, Neelakantan MA. Synthesis and crystal structure of imidazole containing amide as a turn on fluorescent probe for nickel ion in aqueous media. An experimental and theoretical investigation. J Mol Struct 2016;1104:1–6.(d) Wang Z, Cui S, Qiu S, Zhang Z, Pu S. A highly sensitive fluorescent sensor for Zn^{2+} based on diarylethene with an imidazole unit. Spectrochim Acta 2018;205:21–8.(e) Raju V, Selva Kumar R, Tharakeswar Y. Ashok Kumar SKA Multifunctional schiff-base as chromogenic chemosensor for Mn^{2+} and fluorescent chemosensor for Zn^{2+} in semi-aqueous environment. Inorg Chim Acta 2019;493:49–56.

[28] (a) Choi YW, Park GJ, Na YJ, Jo HY, Lee SA, You GR, et al. A Single schiff base molecule for recognizing multiple metal ions: A fluorescence sensor for Zn(II) and Al(III) and colorimetric sensor for Fe(II) and Fe(III). Sens Actuators, B 2014;194: 343–52.(b) Jo TG, Bok KH, Han J, Lim MH, Kim C. Colorimetric detection of Fe^{3+} and Fe^{2+} and sequential fluorescent detection of Al^{3+} and pyrophosphate by an imidazole-based chemosensor in a near-perfect aqueous solution. Dyes Pigments 2017;139:136–47.

[29] (a) Hens A, Maity A, Rajak KKN. *N* coordinating schiff base ligand acting as a fluorescence sensor for zinc(II) and colorimetric sensor for copper(II), and zinc(II) in mixed aqueous media. Inorg Chim Acta 2014;423:408–20.(b) Fu Z-H, Yan L-B, Zhang X, Zhu F-F, Han X-L, Fang J, et al. A Fluorescein-based chemosensor for relay fluorescence recognition of Cu(II) ions and biothiols in water and its applications to a molecular logic gate and living cell imaging. Org Biomol Chem 2017;15:4115–21.(c) Li M, Ruan S, Yang H, Zhang Y, Yang Y, Song J, et al. Nopinone-based AIE-active dual-functional fluorescent chemosensor for Hg^{2+} and Cu^{2+} and its environmental and biological applications. Dalton Trans 2020;49: 15299–309.(d) Abebe F, Gonzalez J, Makins-Dennis K, Shaw R. A New Bis (rhodamine)-based colorimetric chemosensor for Cu^{2+}. Inorg Chem Commun 2020;120:108154.

[30] Ganesan JS, Gandhi S, Radhakrishnan K, Balasubraniem A, Ayyanar S. Execution of juloline based derivative as bifunctional chemosensor for Zn^{2+} and Cu^{2+} ions: Applications in bio-imaging and molecular logic gate. Spectrochim Acta: Mol Biomol Spectrosc 2019;219:33–43.

[31] Lee HL, Lee KH, Lee JY, Lee HJ. Molecular design opening two emission pathways for high efficiency and long lifetime of thermally activated delayed fluorescent organic light-emitting diodes. J Mater Chem C 2021;9:7328–35.

[32] (a) Sahoo A, Baitalik S. Fuzzy logic, artificial neural network, and adaptive neuro-fuzzy inference methodology for soft computation and modeling of ion sensing data of a terpyridyl-imidazole based bifunctional receptor. Front Chem 2022. https://doi.org/10.3389/fchem.2022.864363.(b) Gentile PL. The fuzziness of the molecular world and its perspectives. Molecules 2018;23:2074.

[33] Burchat AF, Chong JM, Nielsen N. Titration of alkyllithiums with a simple reagent to a blue endpoint. J Organomet Chem 1997;542:281–3.

[34] Pena MA, Pérez Sestelo J, Sarandeses LA. Palladium-catalyzed aryl-aryl cross-coupling reaction using ortho-substituted arylindium reagents. J Org Chem 2007; 72:1271–5.

[35] Coulson DR. Tetrakis(triphenylphosphine)palladium(0). Inorg Synth 1971;13: 121–3.

[36] Still WC, Kahn M, Mitra A. Rapid-chromatographic technique for preparative separation with moderate resolution. J Org Chem 1978;43:2923–5.

[37] Melhuish WH. Quantum efficiencies of fluorescence of organic substances: Effect of solvent and concentration of the fluorescent solute. J Phys Chem 1961;65:229–35.

[38] Ma QJ, Zhang XB, Zhao XH, Jin Z, Mao GJ, Shen GL, et al. A highly selective fluorescent probe for Hg^{2+} based on a rhodamine-coumarin conjugate. Anal Chim Acta 2010;663:85–90.

[39] APEX3 version 2016.1. Bruker AXS Inc.; 2016.

[40] SAINT version 8.38A. Bruker AXS Inc.; 2015.

[41] SADABS version 2014/5 (Sheldrick, Bruker AXS Inc.).

[42] Sheldrick GM. SHELXT version 2014/5A**71**. Acta Cryst; 2015. p. 3–8.

[43] Sheldrick GM. SHELXL version 2014/7A64. Acta Cryst; 2008. p. 112–22.

[44] Dolomanov OV, Bourhis LJ, Gildea RJ, Howard JAK, Puschmann H. OLEX2: A complete structure solution, refinement and analysis program. J Appl Crystallogr 2009;42:339–41.

[45] Gaussian 16, rev. B.01. Wallingford, CT: Gaussian, Inc.; 2016.

[46] Tao J, Perdew JP, Staroverov VN, Scuseria GE. Climbing the density functional ladder: nonempirical meta-generalized gradient approximation designed for molecules and solids. Phys Rev Lett 2003;91:146401.

[47] Weigend F, Ahlrichs R. Balanced Basis sets of split valence, triple zeta valence and quadruple zeta valence quality for H to rn: Desing and asseeement of accuracy. Phys Chem Chem Phys 2005;7:3297–305.

[48] Tomasi J, Mennucci B, Cammi R. Quantum mecanical continuum solvation models. Chem Rev 2005;105:2999–3094.

[49] Zhao Y, Truhlar DG. Exploring the limit of accuracy of the global hybrid meta density functional for main-group thermochemistry, kinetics, and noncovalent interactions. J Chem Theor Comput 2008;4:1849–68.

[50] (a) Bauernschmitt R, Ahlrichs R. Treatment of electronic excitations within the adiabatic approximation of time dependent density functional theory. Chem Phys Lett 1996;256:454–64.(b) Stratmann RE, Scuseria GE, Frisch MJ. An efficient implementation of time-dependent density-functional theory for the calculation of excitation energies of large molecules. J Chem Phys 1998;109:8218–24.(c) Casida ME, Jamorski C, Casida KC, Salahub DR. Molecular excitation energies to high-lying bound states from time-dependent density-functional response theory: Characterization and correction of the time-dependent local density approximation ionization threshold. J Chem Phys 1998;108:4439–49.

[51] Iddon B, Lim BL. Metal-halogen exchange reactions of mono- and poly-halogenoimidazoles. J Chem Soc Perkin Trans 1983;1:735–9.